Hydrodynamic Experimental Research on Launch and Underwater Movement of Projectile

Z. T. Diao, D. J. Fang[†] and B. Wang

College of Weaponry Engineering, Naval University of Engineering, Wuhan, Hubei, 430033, China

†Corresponding Author Email:1712021017@nue.edu.cn

ABSTRACT

This study uses a scaled-down model within a proprietary launch tank to address hydrodynamic complexity post-underwater launch. The model addresses the projectile's motion characteristics and flow field during ejection. This exploration encompassed varying ejection pressures, motion characteristics of the launch platform, initial ejection angles, and depths of ejection. The results show that the projectile's residual gas appears as filamentous wake bubbles after underwater ejection, stagnant gas near the tube exit, and bubbles accompanying the projectile. Higher ejection pressure leads to an increase in the volume of stagnant gas at the tube exit, exacerbating the detachment of bubbles accompanying the projectile. When the velocities of the launch platform are V_0 = 0.25 m/s, 0.43 m/s, and 0.48 m/s, the relative attitude angle changes during the projectile's water-exit are 8.60°, 10.69°, and 16.67°, respectively. The bubbles detach more strongly and shrink in size when the projectile is launched with a particular deflection angle. The volume of stagnant gas at the tube exit and bubbles accompanying the projectile notably diminishes as water depth rises under the same ejection pressure.

1. INTRODUCTION

When a projectile is launched underwater, part of the hot, pressurized gas sticks to the projectile's tail, creating tail bubbles. Due to the unstable character of the flow field, the tail bubbles affected by disturbances in the surrounding fluid usually rupture and detach during their contact with the surrounding flow medium. This momentary event results in substantial pressure pulsations, which can impede the continued movement of the projectile. In extreme circumstances, pressure pulses might even cause structural damage, which would make the underwater launch unsuccessful. We call this phenomenon the "gas dynamic aftereffect."

A multitude of elements influence the projectile's hydrodynamics and underwater trajectory. Such as the pressure of the ejection gas, the launch depth, and the initial motion parameters of the submerged launch platform, which include velocity and initial launch angle. When the projectile is ejected from the launch tube, its posture and velocity characteristics are affected by the pressure of the ejection gas and the motion parameters of the launch platform. Furthermore, these variables affect the uniform pressure retention of gas at the tube mouth, which in turn affects the pressure relief of the ejected gas

when the projectile leaves the tube. The initial motion speed and posture of the projectile further affect the hydrodynamics and trajectory of underwater motion after ejection from the launch tube. As the launch depth increases, the impact of the exit parameters on the subsequent motion characteristics becomes more dominant, ultimately determining the motion characteristics of the water exit and influencing on success rate of the launch.

Theoretical derivations and numerical modeling techniques have been a great help for researchers to handle the problems with projectile underwater motion and flow field. Wang et al. (2019) developed a numerical model for the underwater trajectory of the projectile's motion. Through simulation calculations, they derived the changes in the attitude angles of the projectile during vertical entry into the water. Gao and Pan (2020) simulated the underwater trajectories of two projectiles vertically launched with different ejection speeds and time intervals. Zhong and Zhang (2005) derived the trajectory equation for projectiles based on the underwater hydrodynamic characteristics of torpedoes. You et al. (2011) analyzed the impact of different head shapes and surfacing angles on the flow field. Lv (2004) simulated the entire water -exit process of projectiles at various speeds, analyzing the

NOMENCLATURE

ρ_m	density of mixture	λ	thermal conductivity
t	time	c_p	ratio of specific enthalpy to temperature
u_i	velocity components	S_t	strain rate
p	fluid pressure	α_l	volume fraction of the liquid phase
μ_m	dynamic viscosity of the mixture	α_g	volume fraction of gas phase
g_i	gravitational acceleration	V	velocity of liquid–gas mixture
T	temperature	k	turbulent kinetic energy
U	average velocity	μ	dynamic viscosity
β	coefficient of thermal expansion	μ_t	turbulent viscosity
$\overline{F}$	resultant force	$\overline{M}$	resultant moment
G	gravity		

evolution patterns of the attitude angles during water-exit.

In an endless flow field affected by gravity, Basharova et al. (1983) used an approximative system of equations based on the theory of bubbles for thin bodies to determine the form and fundamental dimensions of bubbles along the axis direction.

The projectile could generate bubbles at the tube mouth and the tail after it is launched from the launch tube, and the emergence of these bubbles has a substantial effect on the projectile's underwater speed (Blake et al., 1986). Liu et al.(2005) deployed the finite volume method to investigate the internal flow field of deep-water launch. The results indicate that the rapid expansion of gas flow after ejection leads to the formation of high-temperature gas jets, causing significant damage to the deflector plate. The equations for the two-phase mixture of water and air were solved by Cao et al. (2006) using the finite volume approach. They were able to obtain a coupled solution for the projectile's motion and the two-phase mixture's flow field during the ejection process by employing dynamic mesh technology and independently created programs. Wang et al. (2010) studied the effects of pressure-averaged gas on the projectile's underwater motion characteristics using a multiphase flow model. Liu et al. (2007) solved equations to determine the evolution patterns and fluid dynamic changes of the aeration bubbles surrounding the projectile and utilized vacuolar ventilation technology for the projectile's launch procedure. The findings indicate that aeration bubbles play a significant role in reducing resistance during the projectile's ejection and improving the fluid dynamic loads on the projectile.

Yang et al. (2022) carried out studies in the experimental domain to investigate the projectile's passage over the air-water interface while utilizing active ventilation technology to assist in projectile mobility. Shi et al. (2023) used high-speed cameras to record the evolution of the flow field around the projectile. They carried out a comparative study of the flow field's disturbance properties at various initial deflection angles. Dyment et al. (1998) experimentally investigated the entire process of ejecting a projectile from the tube. Subsequently, numerical methods were incorporated to understand the development of cavities at the projectile's rear. Huang et al. (2013) Zakir used particle image

velocimetry in a water tunnel experiment. They examined the relationship between cavitation instability and swirl and examined the periodic cavitation evolution of a Clark-Y hydrofoil. The findings provide a theoretical basis for analyzing the unsteady cavitation characteristics of projectiles. Zhao et al. (2015) utilized high-speed cameras to observe cavitation development and the motion of projectiles at different speeds. To study how launch speed and depth affect bubble shapes and projectile attitudes, Fu et al. (2018) carried out scale-model experiments. Song et al. (2019) performed water exit experiments with objects of various shapes, highlighting that speed is the primary parameter leading to the deformation of the free liquid surface. Similar to this research, Shi et al. (2020) studied the motion ballistics of projectiles and conducted trajectory experiments of projectiles with asymmetric nose shape entry. They also analyzed the trajectories of projectiles with various initial velocities and water entry angles and proposed a theoretical model of water entry ballistics. In contrast, the study in this work primarily focuses on the evolution features of the gas at the tube mouth and the gas bubbles at the tail during water exit, whereas Shi's study concentrates on the water entrance ballistic properties of projectiles with asymmetric nose shapes.

In conclusion, the current study has made certain findings about the projectile's water trajectory and flow field properties. However there has yet to be much experimental study done; instead, the majority of attention has been on theoretical investigations and numerical simulations. The focus of the majority of research has been on the characteristics of cavitation during projectile motion, with little regard for the evolution patterns of tail bubbles or the impact of gas at the tube mouth. Due to the high costs and extended time frames associated with conducting experiments on the impact of real-size, this paper employed scaled-model ejection experiments to investigate the flow field of tube mouth gas and tail bubbles during the ejection process under different ejection pressures, launch platform motion characteristics, initial ejection angles, and ejection water depths. This study further provides the influence patterns of these parameters on water trajectory characteristics and served as a foundation for subsequent studies on flow control during the ejection of projectiles.

2. NUMERICAL METHOD

2.1 Control Equations

To describe the gas-liquid flow of a projectile launched underwater, the following equation for momentum, continuity, and energy are used, respectively:

$$\frac{\partial(\rho_m u_i u_j)}{\partial x_j} + \frac{\partial(\rho_m u_i)}{\partial t} = -\frac{\partial p}{\partial x_i}$$
$$+\mu_m \frac{\partial}{\partial x_j}(\frac{\partial u_i}{\partial x_j} + \frac{\partial u_j}{\partial x_i}) + \rho_m g_i \tag{1}$$

$$\frac{\partial \rho_m u_i}{\partial x_i} + \frac{\partial \rho_m}{\partial t} = 0 \tag{2}$$

$$\frac{\partial(\rho_m u_i T)}{\partial x_i} + \frac{\partial(\rho_m T)}{\partial t} = \frac{\partial}{\partial x_i}(\frac{\lambda}{c_p}\frac{\partial T}{\partial x_j}) + S_T \tag{3}$$

2.2 VOF Method

The VOF method is an interfacial tracking approach implemented on the Euler domain for two or more insoluble fluid media. The liquid phase is regarded as the primary phase for the gas-liquid two-phase flow problem that this study addresses.

$$\begin{cases} \alpha_l = 0 & gas\ phase \\ 0 < \alpha_l < 1 & gas-liquid\ interface \\ \alpha_l = 0 & liquid\ phase \end{cases} \tag{4}$$

The fluid volume functional equation is given by Equation (5) when the velocity of a moving medium field is $V = (u, v, w)$,

$$\frac{\partial \alpha_l}{\partial t} + \nabla(V\alpha_l) = 0 . \tag{5}$$

Equation (1) states that the density and kinetic viscosity of the mixed medium inside each grid are determined by the weighted average of the medium's phases. The formula for this dependence on values within each grid is as follows:

$$\rho_m = \rho_l \alpha_l + \rho_g \alpha_g \tag{6}$$

For phase q, the basic governing equation for the fluid is provided by the given relation:

$$[\frac{\partial(\alpha_q \rho_q)}{\partial t} + \nabla(\alpha_q \rho_q \vec{v_q})]\frac{1}{\rho_q} = \sum_{p=1}^{n}(m_{pq} - m_{qp}) \tag{7}$$

In Eq. (7), ρ_q, a_q and $\vec{v_q}$ represents density, volume fraction, and velocity of qth phase respectively; m_{qp} represents a mass transfer from the qth phase to the pth phase; and m_{pq} represents a mass transfer from the pth phase to the qth phase.

2.3 SST Turbulence Model

The SST k-ω turbulence model combines the k-w turbulence model for the near-wall surface with the k-ε turbulence model for the far-field, accounting for the anisotropy of turbulence. Here are the transport equations:

$$\nabla(\rho\omega U) + \frac{\partial(\rho\omega)}{\partial t} = \nabla[(\mu + u_t\sigma_\omega)\nabla\omega]$$
$$-\rho\beta f_\beta(\omega^2 - \omega_0^2) + P_\omega + S_\omega \tag{8}$$

$$\nabla(\rho k U) + \frac{\partial(\rho k)}{\partial t} = \nabla[(\mu + \sigma_k\mu_t)\nabla k]\pi$$
$$+\rho\beta^* f_{\beta^*}(\omega_0 k_0 - \omega k) + P_k + S_k \tag{9}$$

where σ_k, σ_ω and β^* are the model coefficients; f_{β^*} is the free shear correction factor; f_β is the vortex extension correction factor; ω is rate of conversion of turbulent kinetic energy into thermal energy; ω_0 and k_0 are the ambient turbulence values. The turbulent viscosity μ_t is defined by the following relation.

$$\mu_t = \frac{\rho a_1 k}{\max(a_1 w, \sqrt{2}S_t F_2)} \tag{10}$$

Where, $a_1 = 0.31$, and F_2 is:

$$F_2 = \tanh(\gamma_2^2) \tag{11}$$

$$\gamma_2 = \max(\frac{500v}{(y^2\omega)}, 2\frac{\sqrt{k}}{\beta^*\omega y}) \tag{12}$$

In Eq. (12), y is the distance from the wall.

2.4 Dynamical Equations of Projectile

The projectile is treated as a rigid body in this research, and its pitch motion is computed after its tail emerges from the tube. Equations (13) and (14) are used to compute the resultant force and moment at the center of mass. Newton's Second Law is used to calculate the projectile's linear acceleration and pitching acceleration. The linear velocity, linear displacement, pitching angular velocity, and pitching angle are then integrated to determine the projectile's final values.

$$\vec{F} = \int_A \vec{\tau}dA + \int_A p\vec{n}dA + \vec{G} \tag{13}$$

$$\vec{M} = \int_A (\vec{r} \times \vec{\tau})dA + \int_A [\vec{r} \times (p\vec{n})]dA \tag{14}$$

where $\int_A p\vec{n}dA$ and $\int_A [\vec{r} \times (p\vec{n})]dA$ are surface pressure integral terms; $\int_A \vec{\tau}dA$ and $\int_A (\vec{r} \times \vec{\tau})dA$ are viscous force integral terms.

3. EXPERIMENTAL PLATFORM AND MODEL

In a launch water tank, model ejection tests were carried out. Figure 1 shows the high-pressure gas ejection mechanism used in the schematic illustration of the experimental apparatus. The launch system, gas supply and regulation device, mobile transportation mechanism, control infrastructure, and data collecting module make up
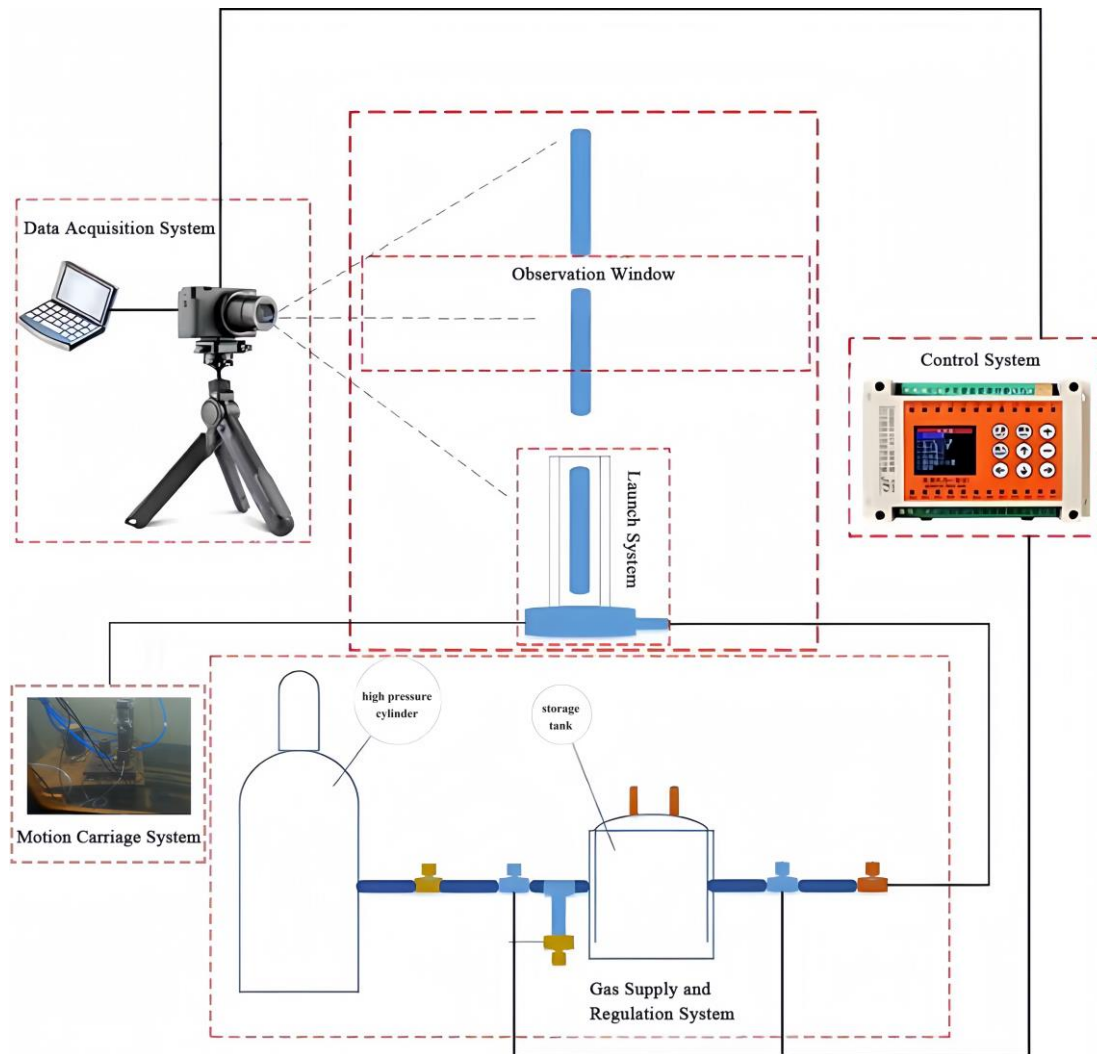
Fig. 1 Schematic diagram of the experiment system

Fig. 2 Experimental water tank

the experimental system. The experimental water tank, provided in Fig. 2, possesses dimensions measuring 3 meters in length, 1 meter in width, and 1.9 meters in height. There are observation windows made of bulletproof glass that are 1.4 meters long and 1.1 meters wide on the front. These windows allow high-speed camera footage to be captured during the launch, capturing

the projectile's complex motion and flow field. The launch speed can be accurately adjusted using the gas pressure in the storage cylinder. Stepping motors are used to drive the carriage, which replicates the launch platform's authentic motion characteristics, while the launch platform itself is fixed on the movable carriage mechanism.

3.1 Launch System

The launch system comprises a launch tube, a base, and a model of the projectile, as shown in Fig. 3. Stainless steel is used to construct the base and launch tube. Bolt connections hold the launch tube to the base. Two threaded holes on the side are closest to the launch tube's bottom. The ejection gas pipeline is connected to one, and a high-frequency pressure sensor is installed on the other to measure bottom pressure variations for the ejection procedure. A movable carriage has the launch base attached to it.

3.2 Gas Supply and Regulation System

The gas supply system provides high-pressure air, which is the source of ejection power. An air compressor, a buffer tank, pipes, and high-speed solenoid valves are all integrated into the gas supply system. In Fig. 4, the air compressor is depicted. The buffer tank is made of

(a) Launch tube

(b) The model of projectile

Fig. 3 Launch System

Fig. 4 Air compressor

Fig. 5 Motion carriage system

Fig. 6 Launch timing control module

stainless steel gas cylinders, and the air compressor can produce up to 1.5 MPa of pressure. Pressure control features on the air compressor's outlet valve make it easier to initially modify the air supply pressure going to the buffer tank. A pressure regulation switch and a high-precision pressure sensor installed in the buffer tank allow for accurate control of the ejection speed by monitoring and regulating the air pressure that is stored. The launch tube and buffer tank are connected by a pipeline that has high-speed solenoid valves on it. To eject the projectile during the launch, gas is injected into the launch tube's base in response to a predetermined opening instruction. To stop the ejection gas flow after the projectile has

successfully exited the launch tube, a time delay program is also put in place.

3.3 Motion Carriage System

The motion carriage system simulates the motion of a submarine throughout the launch process, as shown in Fig. 5. The carriage, motor, guide rail, and gearbox gears are among its essential parts. A waterproof stepper motor powers the carriage platform's power system, and a programmable controller accurately regulates movement distance and speed. A 500 W motor can propel the carriage at a maximum speed of 1.5 m/s and has a smooth speed range of 0 to 500 rpm. Furthermore, shock-absorbing rubber pads are attached to the base of the guide rail to reduce vibrations on the platform and increase the motion stability of the carriage.

3.4 Control System

A programmable logic controller (PLC) and photoelectric switches with a 0.5 m maximum detection range are integrated into the control system. When the carriage approaches the testing window during the experiment and gets within 0.5 meters of the photoelectric switch, the switch recognizes the obstruction with ease. Subsequently, the switch transmits a triggering signal to the PLC, as depicted in Fig. 6. The PLC receives the signal and initiates the electromagnetic valve to open, allowing gas to be transported to the base of the launch tube and
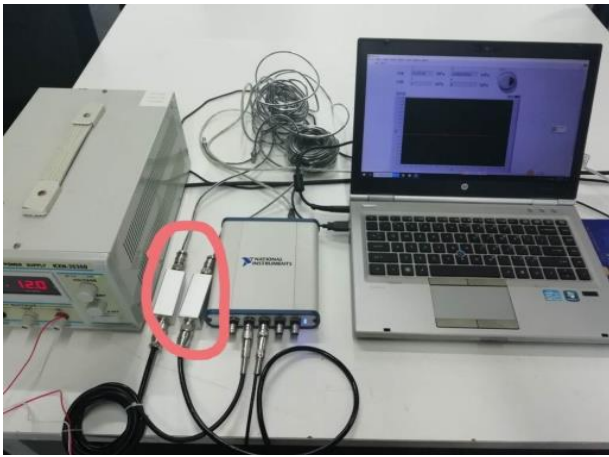
Fig. 7 Data acquisition system

Fig. 8 Schematic diagram of numerical simulation model

ejecting the projectile. Simultaneously, the high-speed camera is activated to capture the projectile's movement and the air-water dynamics during the launch. The electromagnetic valve immediately closes after the projectile is successfully ejected from the tube, thereby cutting off the ejection gas supply. By combining these system features, pressing the launch switch triggers all systems automatically, protecting personnel safety and experimental accuracy.

3.5 Data Acquisition System

The data acquisition system includes a pressure collection system and a high-speed camera, as shown in Fig. 7. A high-frequency dynamic pressure transducer is attached to the side-threaded aperture at the launch tube's base to measure the pressure inside the tube in real-time while it is being ejected. It has a maximum sampling rate of 15 kHz. High-quality imaging data is captured during the ejection process using a VGA-type high-speed camera, which has a maximum capture speed of 1000 frames per second and a resolution of 1280*860 pixels. A high-speed camera records the projectile's complete movement in the water, allowing for the calculation of the projectile's speed and trajectory curves from the captured images. To improve shot clarity, two 200 W LED lights were used as the light source.

A study was conducted to look into the water trajectory and the properties of the flow field under different ejection settings using the devices mentioned above.

It is challenging to obtain precisely comparable pressure curves even with the pressure regulating mechanism in the ejection system. To make sure that the gas storage cylinder's starting pressure remained constant during the ejection operation, the experiment was conducted again for each unique technique. As a vital point of reference, the projectile's tail velocity upon tube exit was observed. If the projectile's speed variance in its depth direction is kept to less than 0.2 m/s in two consecutive experiments with the same launch water depth and angle parameters, the experiment is considered repeatable. The acquired images were subsequently used for the analysis of flow field evolution and motion characteristics.
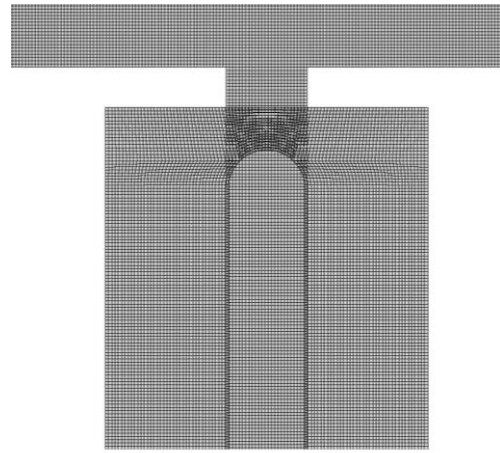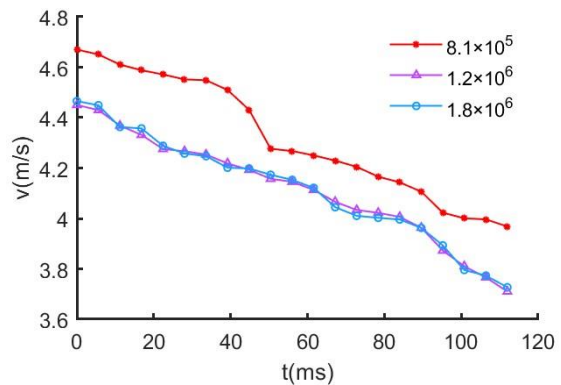

Fig. 9 Velocity variation of the projectile with different grid sizes

3.6 Validation of Experimental Method

A validity test was carried out by running numerical simulations and contrasting the experimental results in this study with those of many other works to confirm the validity of the experimental approach utilized in this work.
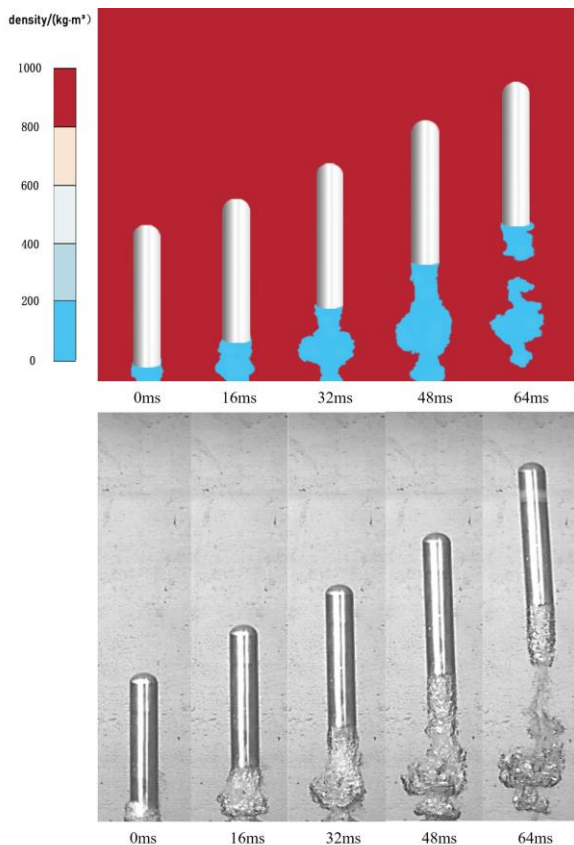
3.6.1 Numerical Simulations

According to the parameters of the experiments in this paper, the simulation model was developed based on the numerical method in Section 2, as shown in Fig. 8.

The projectile's velocity change curves with three different grid numbers, 8.1×10^5, 1.2×10^6, and 1.8×10^6, under a 1.05 MPa ejection pressure are displayed in Fig. 9. It can be seen that the curve of the 8.1×10^5 grids has a large difference with the other two, and the curves of the 1.2×10^6 and 1.8×10^6 grids have a high degree of similarity. The number of 1.2×10^6 grids was finally selected for the numerical simulations.

Figure 10 (a) displays the results of the numerical simulation and the experiment regarding the projectile's velocity change under 1.05 MPa of ejection pressure. The two curves agree well; the experiment's final velocity is 3.78 m/s, while the numerical simulation's final velocity is 3.71 m/s, with a 1.9% error. Fig. 10(b) shows the cloud
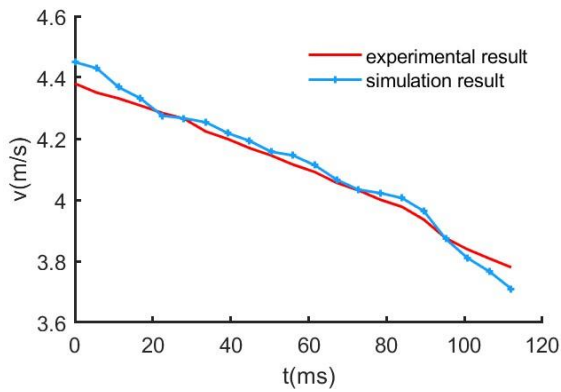
(a) Velocity change curve of the projectile

(b) Cloud diagram of the flow field evolution

Fig. 10 Comparison of simulation result and experimental result

diagram of the flow field evolution under the ejection pressure of 1.05 MPa, and the numerical simulation results agree with the experimental results.

3.6.2 Comparison of Results

As a result, there will inevitably be some differences in the results, particularly in this paper, where the projectile velocity is small and will not cause a cavitation effect around the projectile head, which is the most significant difference from other papers. Other factors that may have contributed to these differences include the size of the scaled-down model, the size of the ejection pressure, the launching water depth, and other parameters that were used in this study.
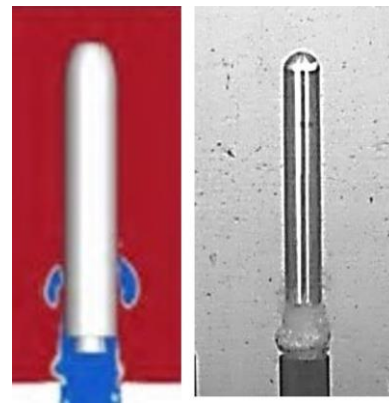
Fig. 11 Comparison of results for vertical launch
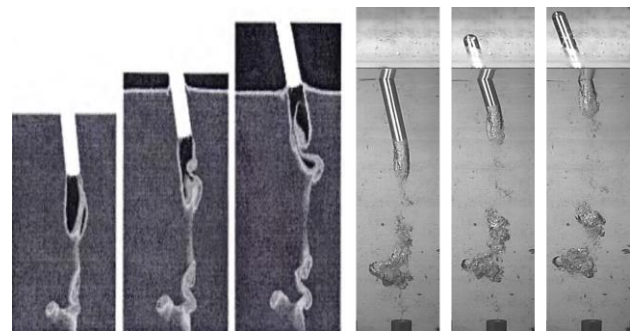

Fig. 12 Comparison of results for projectile with transport velocity

Li et al. (2023) conducted a study on the gas at the tube's mouth using numerical simulation. An experimental setup with a 0.7-meter launch water depth and an ejection pressure of 3 MPa was employed for comparison. As illustrated in Fig. 11, there is a great degree of consistency between the experimental and numerical simulation results regarding the necking phenomenon of the gas at the tube's mouth. The experimental projectile's speed in this paper is less than that of the numerical simulation, and because the projectile's head interacts with the water only weakly, there aren't any large gas clusters in the head, although there are some small gas clusters surrounding the projectile in the numerical simulation.

Numerical simulation of the motion characteristics of a projectile at a certain horizontal initial velocity was conducted by Quan et al. (2014). The experiments in this paper were carried out at a platform velocity of 0. 25 m/s. As can be seen from Fig. 12, there is strong consistency between the evolution phenomena of the shedding bubbles and the bubbles preceding the projectile's tail.

Chen et al. (2021) executed experiments on the projectile's underwater motion and investigated the cavitation effect on the projectile's head. While the study's primary focus differs from this paper's, some of the experimental phenomena also demonstrate the evolution of the gas at the tube's mouth. The experimental projectile in Chen's experiment had an initial velocity of 20 m/s, whereas the experimental projectile in Fig. 13 had an initial velocity of only 5.15 m/s. This velocity
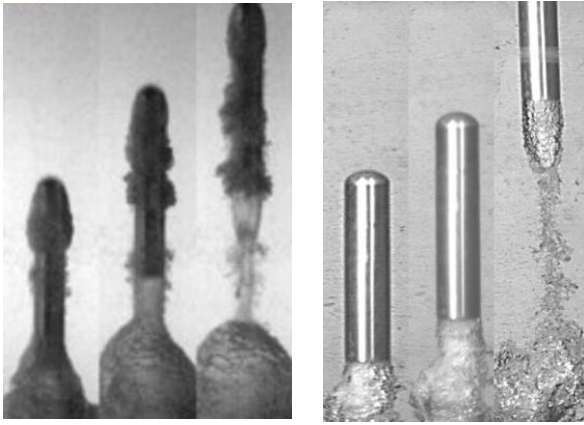
(a) The experiment of **Chen et al. (2021)**

(b) The experiment in this paper

Fig. 13 Comparison of results from different experiments

Fig. 14 Three different pressure curves

Fig. 15 Curves of velocity change

difference significantly affected the size of the gas at the tube mouth, and Chen's experiment had a larger gas cluster volume, which is in line with the analytical conclusions in Section 4.1 of this paper. Based on comparison, it can be observed that despite the variations in gas cluster sizes, there is a significant degree of similarity in their evolution rules. Additionally, all of them have gone through the phases of bubble rupture and necking, as well as the formation of dense gas clusters.

In summary, this paper's conclusions are quite credible because the experiment's validity was confirmed through comparison analysis.

4. RESULTS AND DISCUSSION

4.1 Influence of Ejection Pressure

The projectile's tube exit velocity is significantly impacted by the amount of ejection gas pressure. To overcome the effects of fluid resistance and gravity during underwater motion and ensure a predetermined water-exit speed, a larger launch depth corresponds to a greater tube-exit velocity. This section adjusts the pressure inside the gas storage tank to control the ejection pressure. Examining the projectile's motion properties and the air-water flow field's development under three different ejection pressure scenarios is the goal. The launch depth, H=0.55 m, is the measurement made from the tube mouth to the water's surface. With atmospheric pressure acting as the reference, charts showing the time evolution of three different ejection relative pressures are specifically shown in Fig. 14. Afterwards, the three pressure curves are denoted by the designations $P*_1$, $P*_2$, and $P*_3$, respectively. This research uses the maximum value of the pressure curve as the value of $P*_1$, $P*_2$, and $P*_3$, which is the value of the ejection pressure since it is evident that the entire process of pressure change takes less than 100 ms. The ejection pressures represented by $P*_1$, $P*_2$, and $P*_3$ are 0.84 MPa, 1.05 MPa, and 1.38 MPa, respectively.

4.1.1 Motion Characteristics

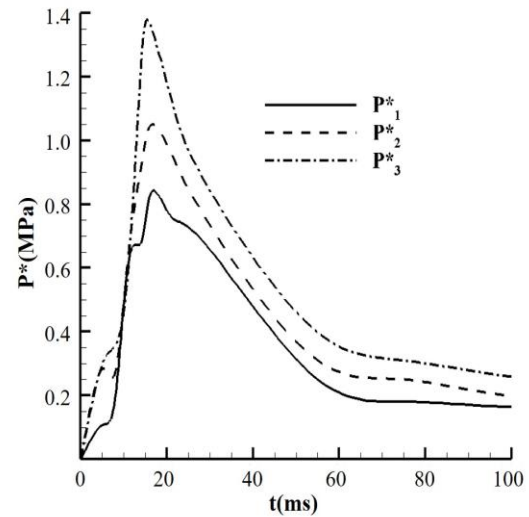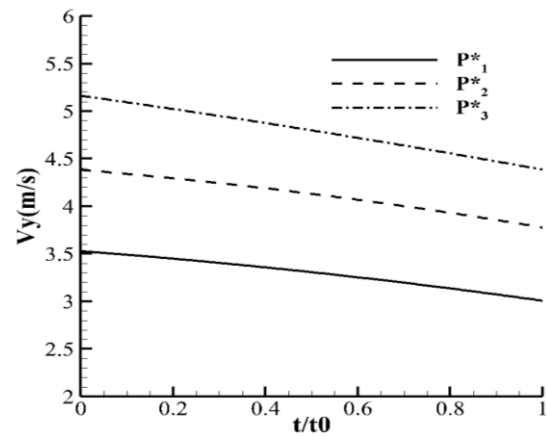The projectile velocity curves for the three ejection

pressure conditions are shown in Fig. 15. When the projectile's tail exits, the launch tube is considered the beginning moment, and when the projectile's head meets the water's surface is considered the ending moment. Higher pressures result in a shorter time of underwater motion because different ejection pressures have different times of underwater motion. To facilitate more thorough comparisons, the graph's time axis is made dimensionless by using the underwater motion time, or t_0, for each case.

At the same water depth, the projectile's tube-exit speed escalates from 3.54 m/s under $P*_1$ to 4.38 m/s under $P*_2$, and further to 5.15 m/s under $P*_3$. The higher tube-exit speeds cause more resistance underwater, which causes the projectile's velocity to decrease more sharply. In the graph, these effects are represented by steeper slopes in the velocity variation with time, together with a larger velocity discrepancy at dimensionless times t/t0=0 and t/t0=1. As the head emerges from the water surface, the velocities under the three ejection pressures are 3.01 m/s, 3.78 m/s, and 4.39 m/s, respectively.

4.1.2 Flow Field Evolution

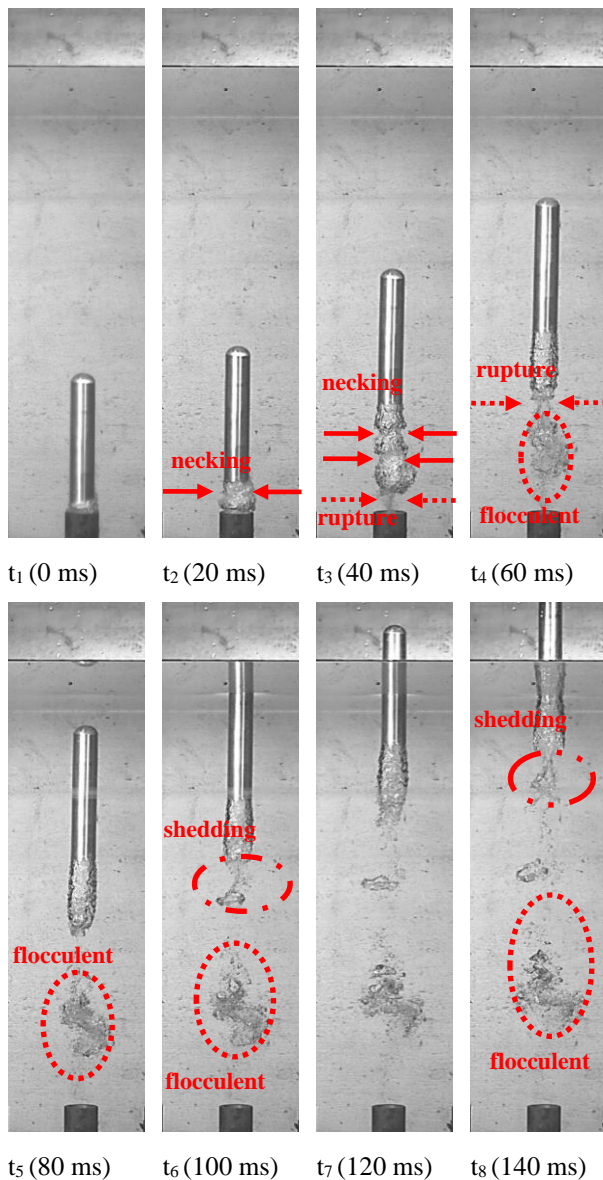The projectile's initial speed and hydrodynamic characteristics

Fig. 16 Projectile motion and bubble evolution at an ejection pressure of P*$_1$

are significantly influenced by the gas evolution at the tube mouth as it leaves the launch tube. The formation of bubbles at ejection pressure P*$_1$ is depicted in Fig. 16. This study primarily selects certain moments of the bubble formation for analysis, designated as t_1 to t_8, in light of changes in underwater motion trajectories and times across distinct settings. The projectile's initial minor deflection angles, gap dimensions, and other local structures, as well as the dynamic evolution of the flow field, all have an impact on the non-symmetric evolution of the bubbles at the tube mouth at the moment of tube exit (t_1) when the discharge of high-pressure gas induces the displacement of water away from the launch tube. At t_2, the bubbles exhibit a noticeable necking phenomenon close to the tube exit, and a depression appears in the middle of the bubbles, away from the tube mouth. The trailing bubbles split into three segments along the projectile's axial path by t_3, indicating that the bubbles near the tube mouth have ruptured significantly and that two separate necking phenomena have emerged in the

middle of the bubbles. The bubble closest to the tube mouth is the largest in terms of both axial and radial dimensions. The bubble at the projectile's tail has the second-smallest volume, and the middle bubble is the smallest. The bubbles near the tube mouth and those at the tail of the projectile have mostly burst by t_4. These bubbles retraction and amalgamation are caused by the compressive force of water, resulting in a general decrease in bubble volume. The mixture of water and air becomes more intense, resulting in a flocculent pattern at the interface between the two variables. Meanwhile, as a result of the projectile's velocity, the tail bubbles undergo significant stretching. As the water depth and atmospheric pressure decrease, the bubbles expand more and more, leading to a significant increase in the axial size of the bubbles.

While the projectile moves towards the water surface (illustrated by the bubble development at moments $t_5 \sim t_8$), the ruptured bubbles near the tube mouth engage in deeper interaction with water. This combination of buoyancy, which drives the bubbles towards the surface of the water, and increased mixing with the surrounding water is what causes this interaction. However, the gas's upward velocity is relatively slow. Simultaneously, a portion of the gas detaches from the tail of the projectile as a result of complex vortices and the shear effect from the air-water interface. This separated segment is traveling upward at a somewhat slower speed than the projectile. This group of bubbles, at last, almost "lingers" close to the tube outlet. The impact of this gas cluster on the subsequent development of the associated bubbles and the projectile's hydrodynamics is negligible as the projectile moves away from the tube exit. Since the bubbles' axial sizes are getting smaller, they are constantly losing their tail bubbles and combining with water. The phenomenon of the tail bubbles blending with the water is more noticeable the closer the projectile's tail is to the water's surface.

Figures 17 and 18 depict the flow field of the projectile from the tube exit to the water exit under ejection pressures P*$_2$ and P*$_3$, respectively. The comparison at time t_2 in Figs. 17 and 18 shows that during the early stages of tube exit, an increase in ejection pressure highlights the pressure relief at the tube exit, and the radial dimension of the bubbles close to the tube mouth likewise grows. The sudden discharge of high-pressure gas from the tube exit causes the bubbles to evolve dynamically in a complex way, giving the bubbles an asymmetrical shape. Specifically, the pressure relief and bubble shapes become increasingly complex as the ejection pressure increases. The necking phenomenon appears in the middle of bubbles close to the tube mouth and at a distance from the tube mouth during the early stages of tube exit under the three pressure settings. The bubbles that follow the bullet burst as it moves forward, creating two separate sections in the water. The first is the bubble that remains in the tube mouth; it is distinguished by its slower velocity, stronger mixing with water, and obvious energy loss. The other component is the bubble that follows the projectile's tail and travels in unison with it. This part of the bubbles disperses in the water and keeps breaking off during its development to form different flocculent gas clusters. The number of bubbles remaining in the tube mouth increases
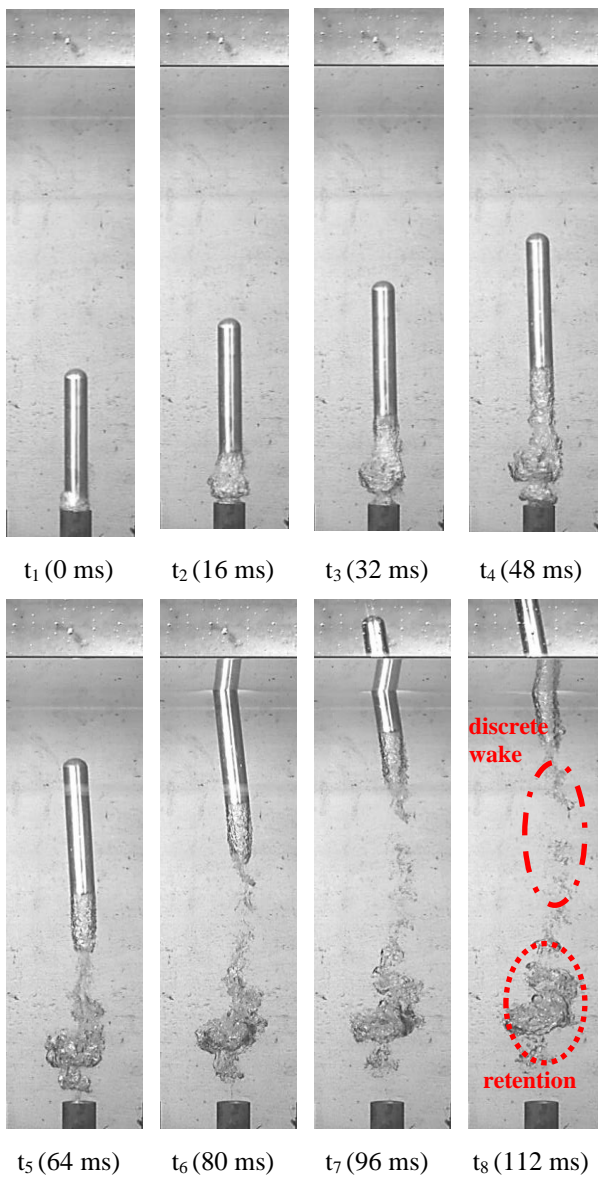
t₁ (0 ms)   t₂ (16 ms)   t₃ (32 ms)   t₄ (48 ms)

t₅ (64 ms)   t₆ (80 ms)   t₇ (96 ms)   t₈ (112 ms)

Fig. 17 Projectile motion and bubble evolution at an ejection pressure of P*₂

t₁ (0 ms)   t₂ (14 ms)   t₃ (28 ms)   t₄ (42 ms)

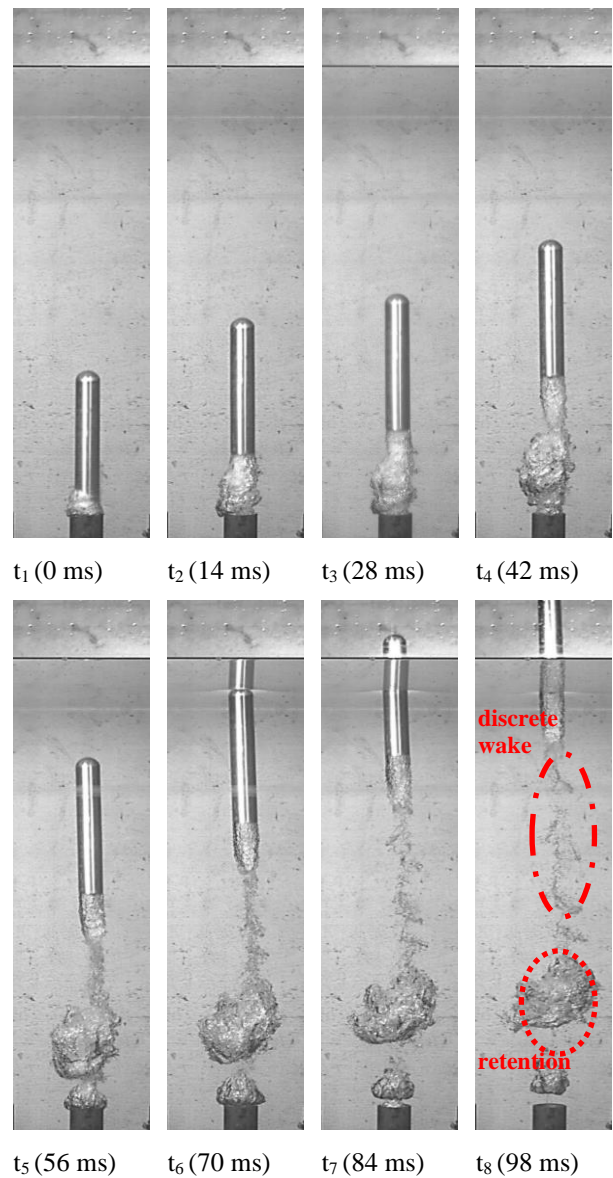t₅ (56 ms)   t₆ (70 ms)   t₇ (84 ms)   t₈ (98 ms)

Fig. 18 Projectile motion and bubble evolution at an ejection pressure of P*₃

with pressure, and the loose trail of bubbles following the projectile's tail becomes more noticeable. At P*₃ pressure, even after closing the ejection gas source, a relatively small-volume gas cluster remains near the tube mouth. This phenomenon is associated with the elevation of gas volume within the tube under high-pressure conditions.

It is noteworthy that as the ejection pressure rises, the volume of the bubbles trailing the tail of the projectile markedly diminishes. This trend is evident in the bubbles' evolution from t₅ to t₈, depicted in Fig. 16 to Fig. 18. There are two main causes for this phenomenon: first, a higher ejection pressure causes a bigger volume of stagnant bubbles at the tube mouth. Once the bubbles have contracted or burst, a significant volume of gas enters the stagnant bubbles. Second, as the projectile moves faster due to an increase in ejection pressure, the bubbles move faster as well. This increases the shear effect during the bubbles' relative motion with water and causes a larger number of flocculent bubbles to descend along the water trajectory.

4.2 Influence of Platform Motion Speed

The movement of the launch platform throughout the underwater launch process has a major impact on the hydrodynamic properties and flow field evolution of the projectile. The projectile's initial deflection characteristics are influenced by the current flowing through it. On the downstream side of the projectile, gas at the tube mouth concentrates, making it easier for the ejection gas to release pressure in that area. Consequently, it affects the evolution of trailing bubbles and the development of water trajectory. Here, three distinct platform velocities (0.25 m/s, 0.45 m/s, and 0.48 m/s) are investigated, the distance from the tube mouth to the water surface is H = 0.55 m, and the ejection pressure is taken as P*₂ from the previous paper.

4.2.1   Motion Characteristics

The projectile's trajectory changes from the time the tail leaves the tube opening until the head leaves the water's surface, as seen in Fig. 19. Since it has the same
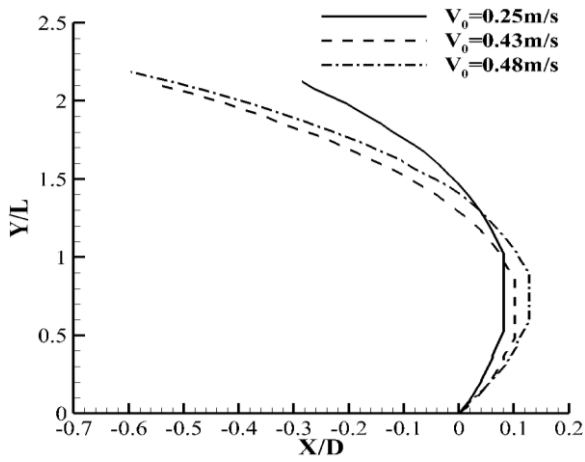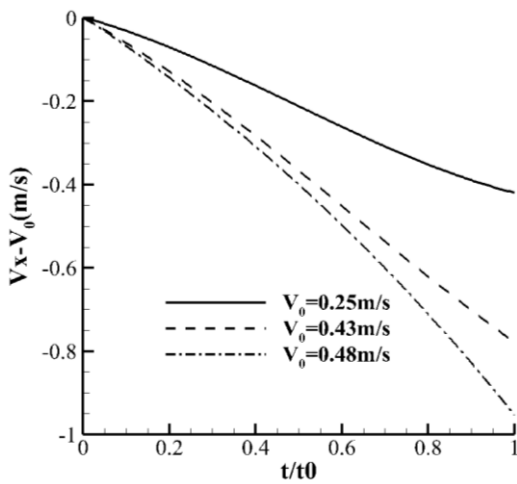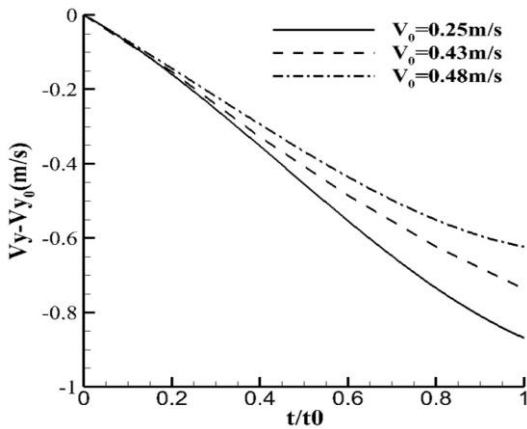
Fig. 19 Trajectory of the projectile

(a) Horizontal velocity

(b) Velocity along the water depth
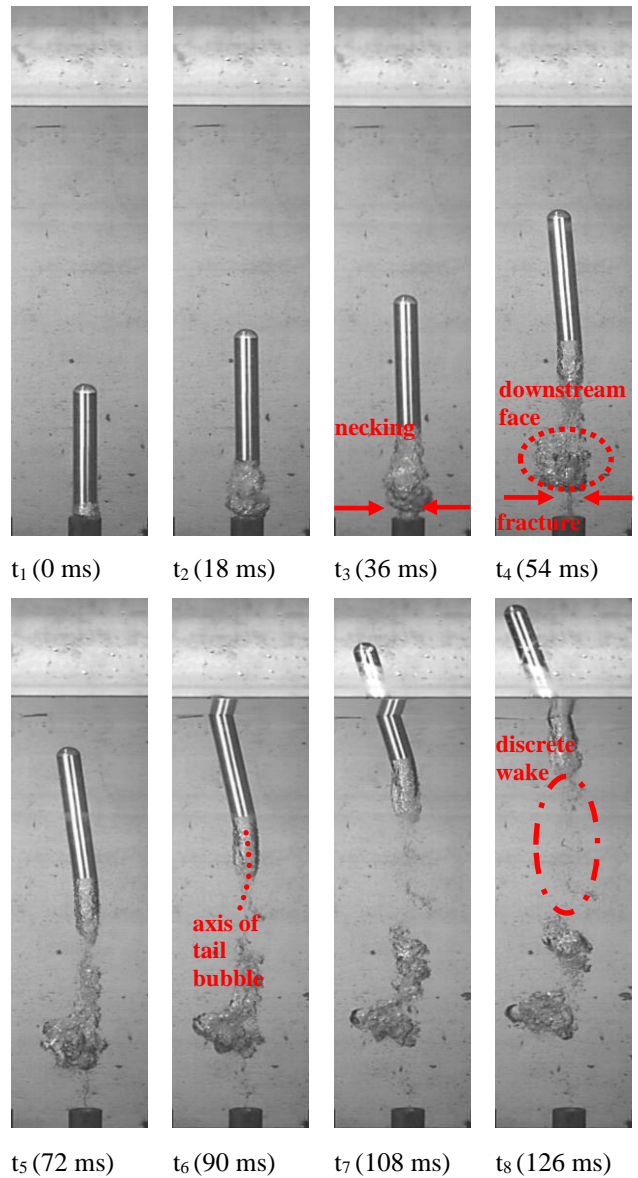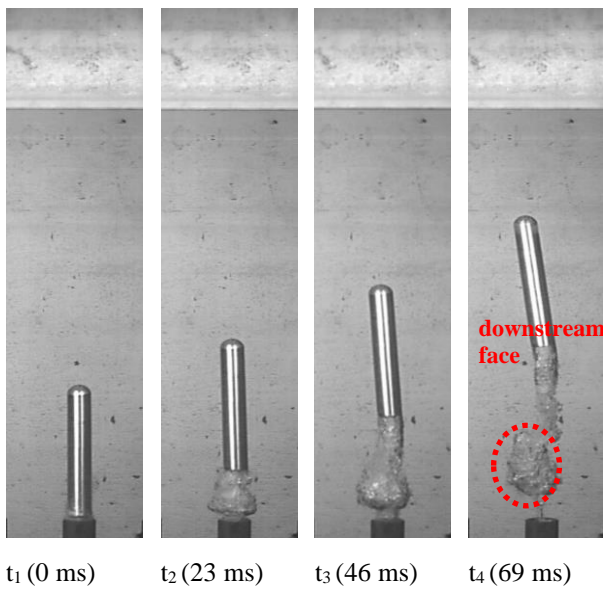
Fig. 20 Velocity change curve of the projectile

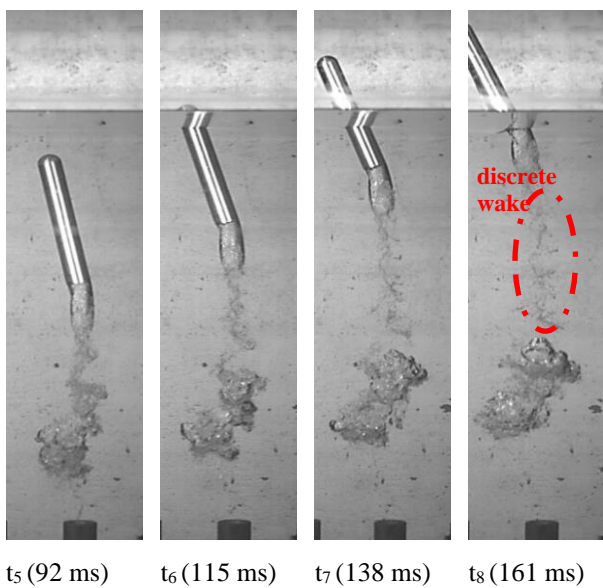**Fig. 21 Platform moves with a speed of V0 = 0.25 m/s**

horizontal velocity as a result of the relative contact and obstruction from the water flow. Eventually, the projectile will move in the opposite direction to the platform and leave the water surface.

The time from the head out of the water to the tail out of the tube serves as a reference quantity for dimensionless time, and Fig. 20 (a) shows the curve of horizontal relative velocity to the moving platform with dimensionless time. The greater the initial platform velocity, the faster the deceleration in that direction, which is due to the greater fluid resistance, as depicted in Fig. 20.

The dimensionless velocity variation along the direction of water depth is illustrated in Fig. 20 (b). As seen in Fig. 21 to Fig. 23, a higher initial platform velocity increases the deflection moment on the projectile, resulting in a bigger deflection angle. As a result, the projectile's water-exit velocity decreases, and resistance increases in the direction of the water's depth.

beginning horizontal velocity, it is evident that the projectile continues to proceed in the direction of the platform after exiting the launch tube. The projectile moves farther in the direction of the platform with a higher platform velocity. However, there is a notable attitude deflection and a sharp decrease in the projectile's

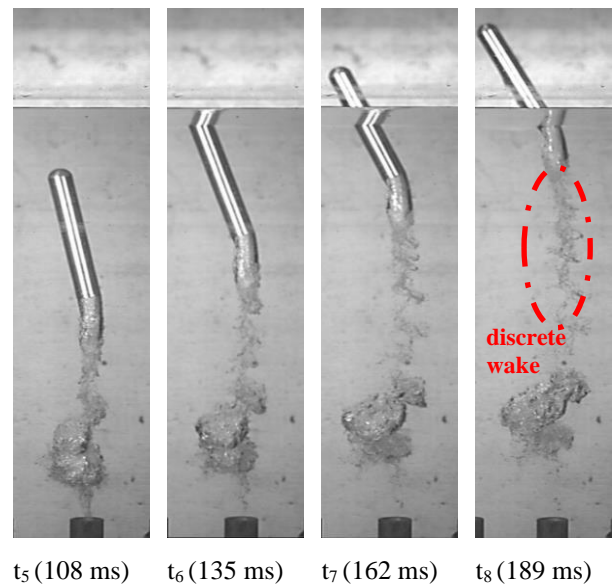t₁ (0 ms)   t₂ (23 ms)   t₃ (46 ms)   t₄ (69 ms)

t₅ (92 ms)   t₆ (115 ms)   t₇ (138 ms)   t₈ (161 ms)

Fig. 22 Platform moves with a speed of V0 = 0.43 m/s
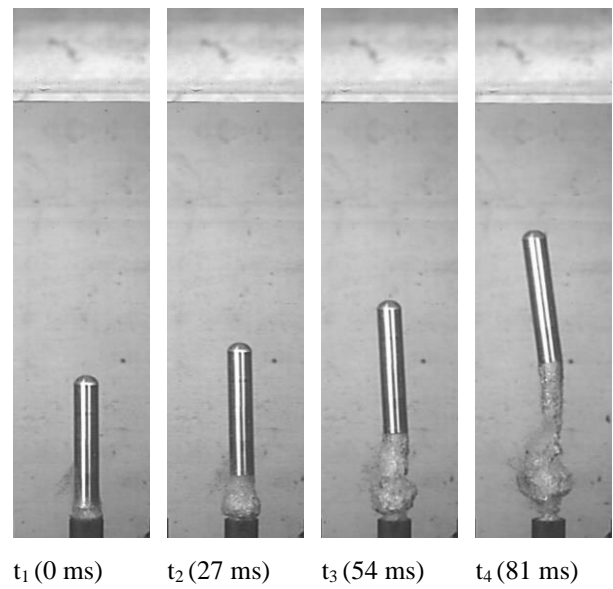
t₁ (0 ms)   t₂ (27 ms)   t₃ (54 ms)   t₄ (81 ms)

t₅ (108 ms)   t₆ (135 ms)   t₇ (162 ms)   t₈ (189 ms)

Fig. 23 Platform moves with a speed of V0 = 0.48 m/s

4.2.2 Flow Field Evolution

The characteristics of flow field evolution under three different platform speeds are shown in Fig. 21 ~ Fig. 23. When the ejection pressure is the same, the launch tube's initial velocity of relief airflow is significantly higher than the platform's movement speed. This results in bubbles at the tube mouth that have a similar shape in the early stage (as seen in the t_1 moment). More noticeable bubble growth occurs on the downstream face (left side in the figures) as the projectile's tail leaves the tube due to collision and resistance from the relative water flow.

There is initially minimal variation in the bullet's initial deflection as the tail of the projectile emerges from the tube. The projectile's subsequent deflection, however, increases rapidly because of the asymmetry of the tail bubbles and the varied beginning flow velocities. The projectile's angle of attack against the current will increase as the initial platform speed increases because of the greater relative impact of the incoming flow. Additionally,

the pressure on the projectile's upstream face will be greater than that on its downstream face, resulting in a larger deflecting moment—an anticlockwise moment in Fig. 21~Fig. 23. Moreover, the tail bubbles that follow bear a stronger effect, focusing mostly on the downstream face. The launch tube's relatively high gas pressure causes bubbles to evacuate with greater impact force, which causes an anticlockwise moment to occur on the projectile's tail. Consequently, under the combined effects of these two factors, the deflection angle of the projectile increases with the initial horizontal velocity.

The bullet's accompanying bubbles clearly show bending and distortion as the projectile moves and deflects underwater. Whereas bubbles nearer the projectile's tail have a comparable orientation to the projectile, bubbles farther from the projectile's tail display a more vertical posture. The projectile's bubbles exhibit a more prominent distortion in direct proportion to its underwater deflection angle. Furthermore, as a result of the projectile's deflection and horizontal motion, the water flow's lateral
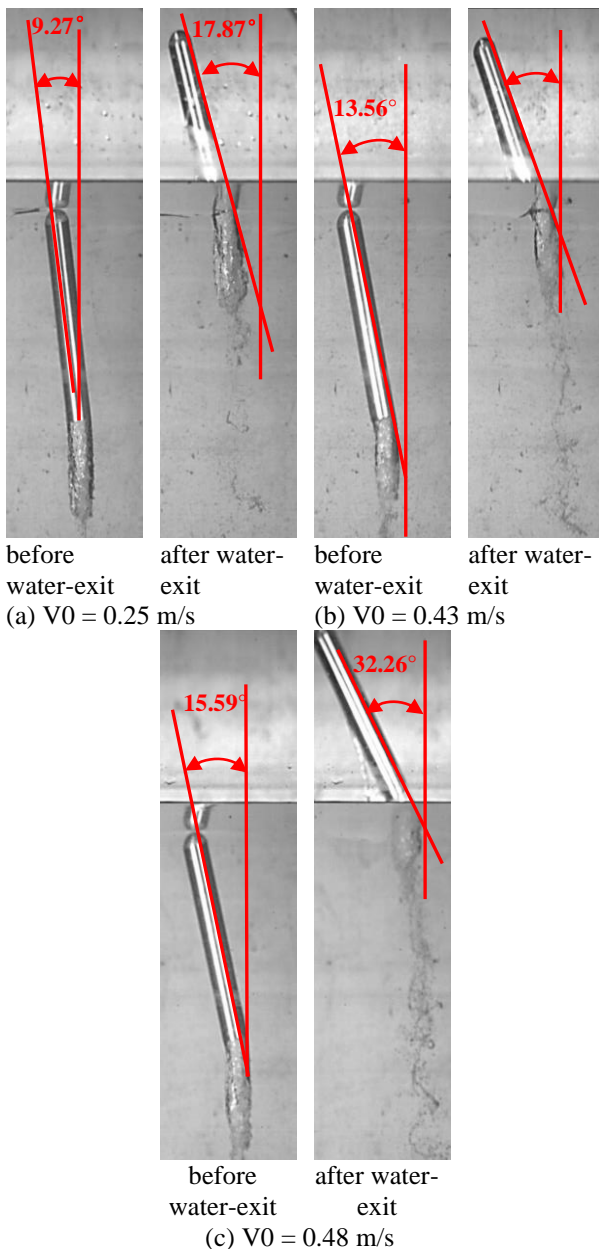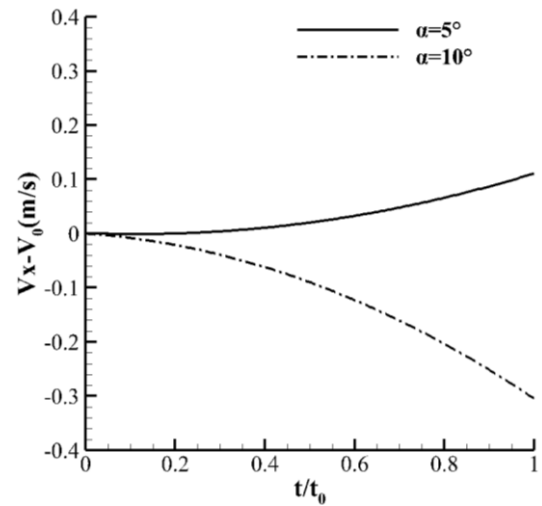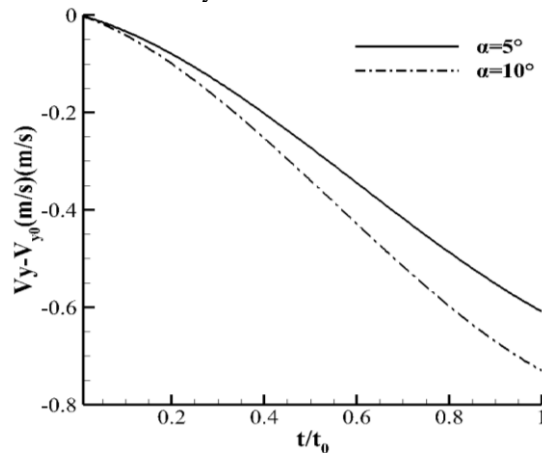
before water-exit / after water-exit
(a) V0 = 0.25 m/s

before water-exit / after water-exit
(b) V0 = 0.43 m/s

before water-exit / after water-exit
(c) V0 = 0.48 m/s

Fig. 24 Comparison of attitudes before and after exiting the water with different platform movement speeds

(a) Horizontal velocity

(b) Velocity along the water depth
Fig. 25 Velocity characteristics of the projectile

influence on the tail bubbles gets stronger. Consequently, this intensifies the mixing and detachment of the bubbles accompanying the projectile, as shown at moment t_7 in Fig. 21~Fig. 23. The greater the deflection of the projectile, the smaller the axial length of the bubbles accompanying the projectile, and the more pronounced the flocculent wake shed in the water.

The projectile's underwater motion posture is significantly altered by the initial platform speed, as was previously examined. The abrupt fluid medium transition also causes a noticeable fluctuation in the hydrodynamic forces and moments that the projectile experiences during the water-exit process. It is observable that although the water-exit time is brief, the deflection angle of the projectile experiences a rapid increase, as presented in Fig. 24. The higher the initial speed of the projectile along the horizontal direction, the more pronounced the deflection

angle during the underwater movement. When the initial speeds of the projectile along the horizontal direction are V0 = 0.25 m/s, 0.43 m/s, and 0.48 m/s, respectively, the deflection angle at the moment of the projectile's head exiting water is 9.27°, 13.56°, and 15.59° respectively, and the deflection angles at the moment of projectile's tail exiting water are 17.87°, 24.25°, and 32.26° respectively. That is, the relative changes in attitude angle during water exit are 8.60°, 10.69°, and 16.67°, respectively. Therefore, the projectile's posture at the moment of the tail entering the water can be greatly enhanced by carefully minimizing the deflection angle.

4.3 Influence of Initial Deflection Angle

Achieving a completely vertical launch in real-world scenarios is challenging due to the influence of ocean currents and the movement characteristics of the submarine. This can have an impact on the trajectory and flow field evolution of the fired projectile. Subsequently, this study carried out the experiments under three conditions with initial launch angles α = 0°, 5° and 10°. The launch depth is H = 0.55 m, and the ejection pressure is taken as $P*_2$ from the previous paper.

4.3.1 Motion Characteristics

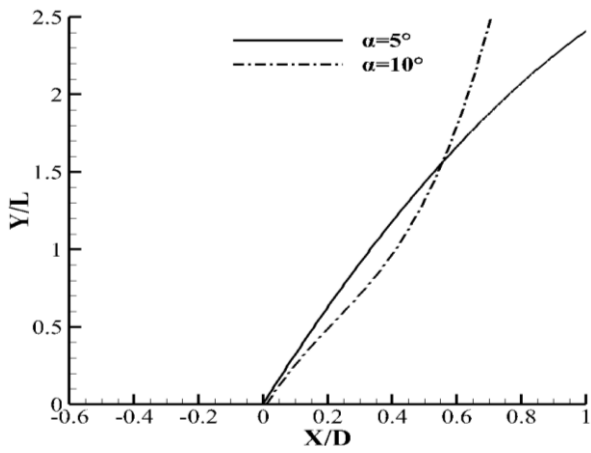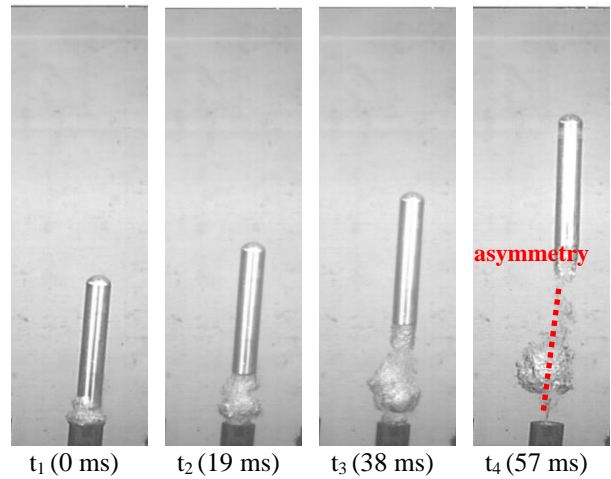The variation in velocity with dimensionless time during the launch process is shown in Fig. 25, revealing
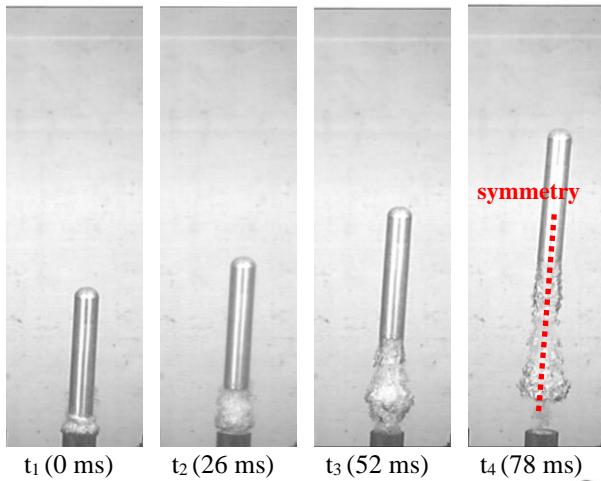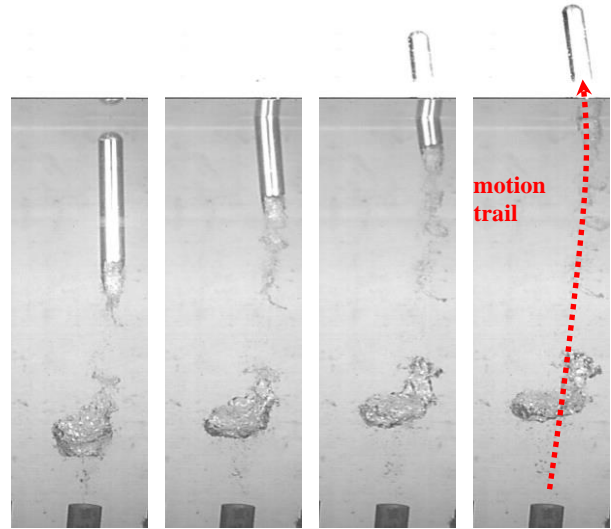
Fig. 26 Dimensionless ballistic change

t_1 (0 ms) t_2 (19 ms) t_3 (38 ms) t_4 (57 ms)

t_5 (76 ms) t_6 (95 ms) t_7 (114 ms) t_8 (133 ms)

Fig. 28 Initial deflection angle is α = 10°

t_1 (0 ms) t_2 (26 ms) t_3 (52 ms) t_4 (78 ms)
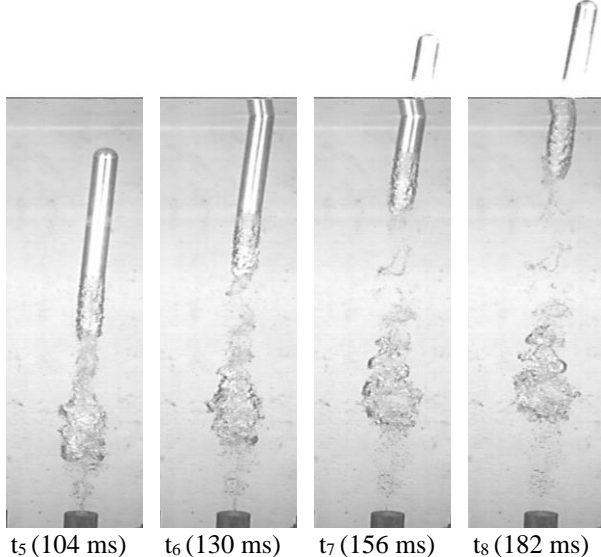
t_5 (104 ms) t_6 (130 ms) t_7 (156 ms) t_8 (182 ms)

Fig. 27 Initial deflection angle is α = 5°

that the change in velocity along the horizontal at the two angles is very different when the initial deflection angle is α = 5°. The projectile's horizontal velocity increases over time, whereas at an initial deflection angle of α = 10°, the horizontal velocity of the projectile gradually decreases.

When α = 10°, there is a more noticeable slowdown of the underwater trajectory segment in terms of velocity change along the direction of water depth. This is because of variations in horizontal velocity, which cause the trajectory to eventually reverse, as illustrated in Fig. 26.

4.3.2 Flow Field Evolution

As can be seen from Fig. 27 to Fig. 28, which depict the projectile's path and the evolution of the bubbles under different starting deflection angles, the launch tube's quick initial outflow speed reduces the effect of buoyancy on the bubble morphologies after the tube is deflected. The morphological distribution of the bubbles at the tube mouth along the launch tube's axis is similar to that seen in Fig. 17 above in the absence of attitude deflection. As the projectile moves away from the launch tube, with a small initial deflection angle (α = 5° in Fig. 27), the projectile undergoes a relatively minor attitude change during the motion process, resulting in a more symmetrical development of stagnant bubbles near the tube mouth and bubbles accompanying the projectile' tail.

When the initial deflection angle rises to α=10° (as illustrated in Fig. 28), the hydrodynamic correction effect
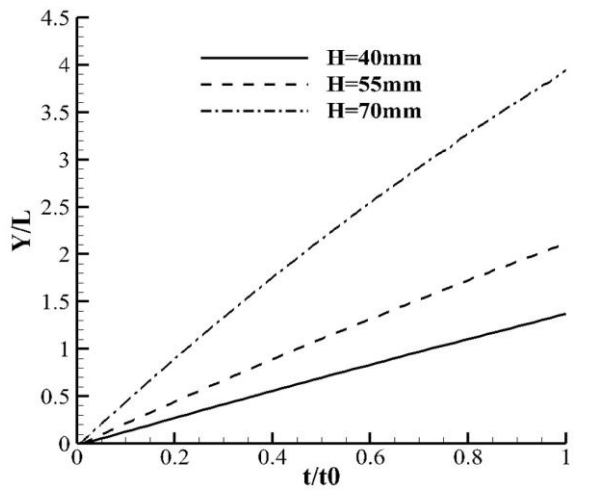
(a) Dimensionless ballistic change
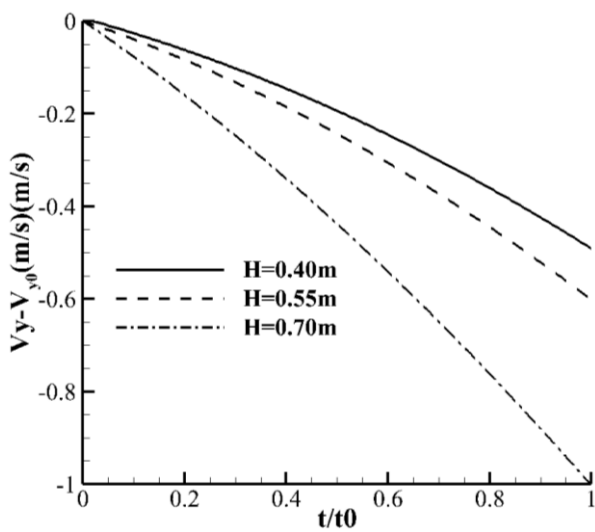
(b) Relative change in velocity

Fig. 29 Movement characteristics of the projectile

t_1 (0 ms) t_2 (4 ms) t_3 (8 ms) t_4 (12 ms)

t_5 (16 ms) t_6 (20 ms) t_7 (24 ms) t_8 (28 ms)

Fig. 30 Ejection water depth H = 0.40 m

to the center of mass becomes more significant the larger the projectile's deflection angle, as the projectile's deflection angle decreases because the center of buoyancy is situated in front of the center of mass. The projectile deflects its attitude and then takes on an angle of attack about the incoming flow. This angle of attack increases the correction moment and increases the projectile's angular velocity of deflection and deflection angle, which in turn affects the formation and evolution of bubbles. After the deflection of the projectile, the tail bubbles stretch fracture is advanced, as shown by the bubble development at moments $t_1 \sim t_4$ in Fig. 27 and Fig. 28. Thereafter, the stationary bubbles close to the tube mouth get bigger, while the bubbles associated with the projectile's tail get considerably smaller. The accompanying bubbles near the projectile's tail gradually separate and shrink in size as the bullet deflects, becoming more noticeable throughout the process. This aligns with the earlier analysis under different launch platform speeds, highlighting that a substantial change in the projectile's attitude will result in an intensified detachment of the bubbles accompanying the projectile's tail and a reduction in the size of the bubbles.
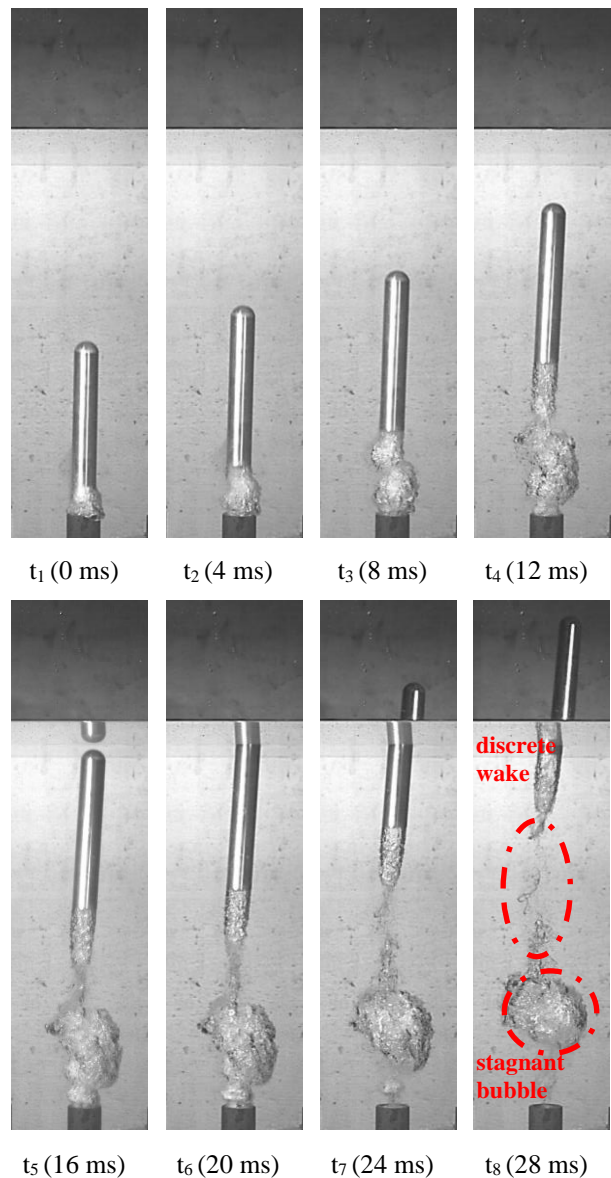
4.4 Influence of Launching Water Depth

The investigation of underwater motion and flow field evolution characteristics of the projectile at three distinct water depths (H = 0.4 m, 0.55 m, and 0.70 m), with a fixed ejection gas pressure of P*Max = 3 MPa, while the launch platform remains stationary.

4.4.1 Motion Characteristics

The projectile decelerates more noticeably with increasing water depth when the ejection pressure stays constant, as can be seen by looking at the dimensionless displacement and relative changes in velocity shown in Fig. 29 (a) and Fig. 29 (b). This can be attributed to a rise in head resistance due to an increase in the local water pressure within the head. The rise in water depth after the projectile's tail exits the tube causes an increase in ambient water pressure, which in turn causes an increase in the internal pressure of the tail bubbles. However, this increase in pressure was insufficient to appreciably alter the projectile's tendency to slow down. As evidenced by Fig. 29(b), the relative decrease in speed increases
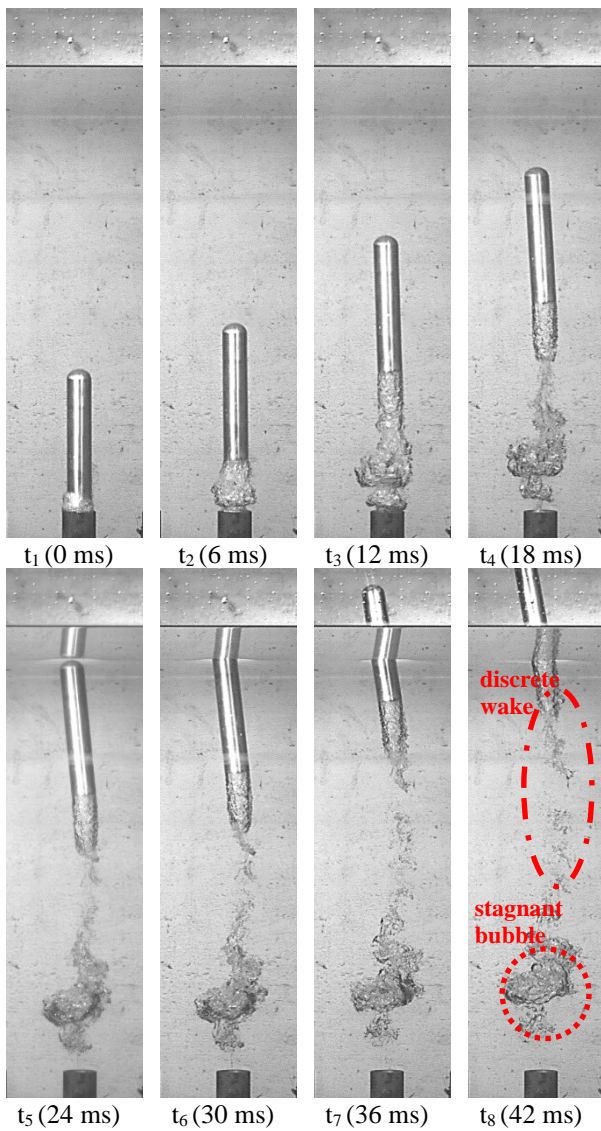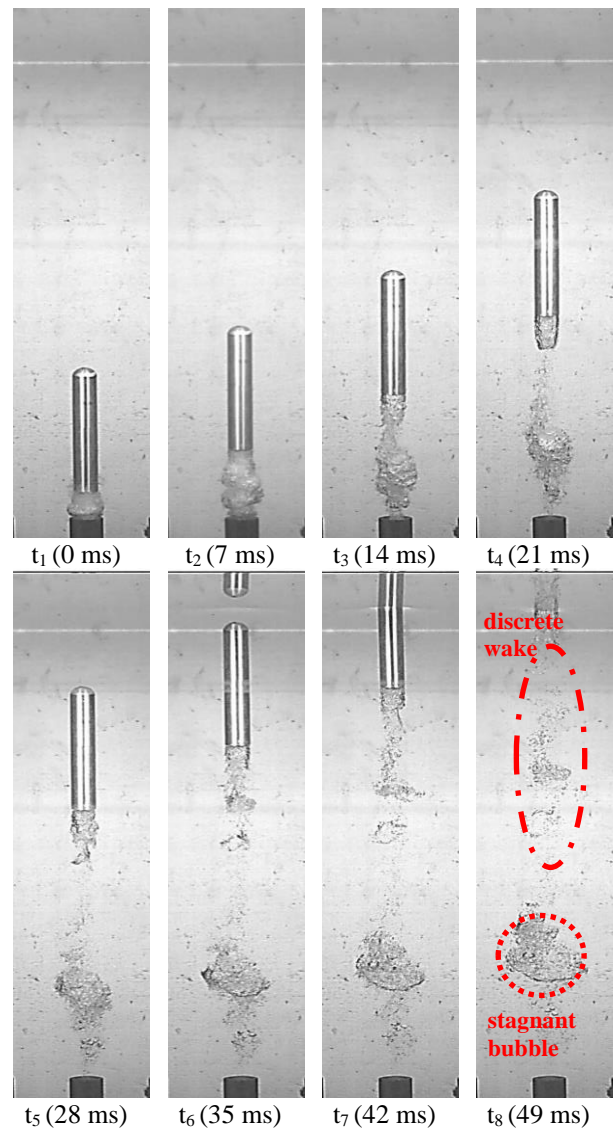
Fig. 31 Ejection water depth H = 0.55 m

Fig. 32 Ejection water depth H = 0.70 m

significantly in comparison to the increase from H = 0.4 m to H = 0.55 m when the launch depth increases from H = 0.55 m to H = 0.70 m. This is because the tail bubbles' pressure is much less than the head stagnation pressure when the tail bubbles undergo the pressure relief of tube mouth and expansion. Furthermore, at increased depth, the duration of underwater travel extends, accentuating the deceleration effect.

4.4.2 Flow Field Evolution

As demonstrated in Fig. 30~Fig. 32, when the water depth varies, the ejection gas pressure stays constant, but the relative pressure between the gas pressure inside the tube and the ambient water pressure at the tube mouth is certain to differ. This will have an impact on the projectile's motion characteristics and the formation of bubbles. The expansion of the bubbles when pressure is released from the tube mouth is weakened as the water depth increases because of the rise in ambient water pressure; in other words, the greater the water depth, the smaller the bubbles are near the tube mouth with the same ejection pressure.

Additionally, as was already mentioned, the projectile's

longer water ballistic in the deep water causes the bubbles it is accompanied by to be subjected to the shear action of the water current for a longer time and distance. As a result, more flocculent bubbles fall off, and the volume of the bubbles is also smaller when the projectile's tail emerges from the water. It's interesting to notice that the projectile's underwater trajectory segment bears a particular beginning deflection angle, which is determined by the initial installation angle, but this has no bearing on the flow field's main dynamics.

CONCLUSION

This study explored the impact of varying ejection pressures, platform velocities, initial ejection angles, and water depths on the flow field evolution and motion characteristics of the projectile. Here are the principal conclusions:

(1) During the underwater ejection process, the remaining gas separates into three components in the water: the tube mouth's static gas, the projectile's bubbles, and the filamentous wake bubbles that break apart along the trajectory. The stagnant gas close to the tube mouth

has very little upward velocity. As the projectile moves farther from the tube mouth, its impact on the projectile's hydrodynamics and motion decreases.

(2) The greater the ejection pressure, the larger the volume of the stagnant gas near the tube mouth. Nonetheless, owing to the heightened underwater motion velocity of the projectile, the detachment of the tail bubbles intensifies, and the volume of the tail bubbles markedly diminishes upon water exit. A particular initial deflection angle displayed by the launch platform or projectile causes the projectile's attitude to alter more noticeably in the water section. It also causes the tail bubbles to separate more widely and shrink in size, which causes the projectile's subsequent attitude to change dramatically. The volume of the stagnant gas near the tube mouth and the bubbles that accompany the projectile upon water exit significantly decrease as the water depth increases, under equivalent ejection pressure conditions. This means that the initial attitude deflection has a greater influence on the projectile's water exit posture.

(3) When the initial speeds of the projectile along the horizontal direction are V0 = 0.25 m/s, 0.43 m/s, and 0.48 m/s, the relative changes in attitude angle of the projectile during water exit are 8.60°, 10.69°, and 16.67° respectively. The sudden change in medium density and wetted area that occurs as the projectile crosses the free interface affects its hydrodynamic properties. The projectile's velocity and attitude change quickly, especially if it shoots out of the water at an acute angle. This leads to more noticeable changes in the projectile's motion characteristics and could lead to a launch failure.

(4) The deep water effect, complex oceanic conditions, and the launch platform's initial motion characteristics (velocity and launch angle) will all cause significant changes in the projectile's attitude and hydrodynamics during its underwater movement and water-exit, and the flow field's evolution during air-water interactions will be more complicated. It is advisable to implement appropriate flow control measures to refine the fluid dynamics features of the projectile and to strengthen the stability of the water exit attitude.

CONFLICT OF INTEREST

We declare that we have no known competing financial interests or personal relationships that could have appeared to influence the work reported in this paper.

AUTHORS CONTRIBUTION

Z. T. Diao: conceptualization, methodology, data curation, formal analysis, writing the original draft. **D. J. Fang**: conceptualization, methodology, manuscript revision, investigation. **B. Wang:** resources, supervision, editing, formal analysis.

REFERENCES

Basharova, V. N., Serebryakov, V. V., & Buivol, V. N. (1983). Slender axisymmetric cavities in the flow around bodies in a longitudinal gravity force field. *Soviet Applied Mechanics, 19*(4), 359–366. https://doi.org/10.1007/BF00884867

Blake, J. R., Taib, B. B., & Doherty, G. (1986). Transient cavities near boundaries. Part 1: Rigid boundary. *Journal of Fluid Mechanics, 170*, 479-497. https://doi.org/10.1017/S0022112086000988

Cao, J., Lu, C., Li, J., & Wu, L. (2006). Study on the underwater vertical self-launching process of submarine-launched missiles. *Hydrodynamics Research and Progress: Series A, 21*(6), 752-759. https://doi.orh/10.3969/j.issn.1000-4874.2006.06.010

Chen, S., Shi, Y., Pan, G., & Gao, S. (2021). Experimental research on cavitation evolution and movement characteristics of the projectile during vertical launching. *Journal of Marine Science and Engineering, 9*(12), 1359. https://doi.org/10.3390/jmse9121359

Dyment, A., Flodrops, J. P., Paquet, J. B., Dupuis, D., & Marchand, D. (1998). Gaseous cavity at the base of an underwater projectile. *Aerospace Science and Technology, 2*(8), 489–504. https://doi.org/10.1016/S1270-9638(99)80008-X

Fu, G., Zhao, J., Sun, L., & Lu, Y. (2018). Experimental investigation of the characteristics of an artificial cavity during the water-exit of a slender body. *Journal of Marine Science and Application, 17*, 578-584. https://doi.org/10.1007/s11804-018-00055-5

Gao, S., & Pan, G. (2020). Study on the characteristics of simultaneous unsteady current field. *Digital Ocean and Underwater Attack and Defense, 3*(3), 271-275. https://doi.org/10.19838/j.issn.2096-5753.2020.03.016

Huang, B., Young, Y. L., Wang, G., & Shyy, W. (2013). Combined experimental and computational investigation of unsteady structure of sheet/cloud cavitation. *Journal of Fluids Engineering, Transactions of the ASME, 135*(7). https://doi.org/10.1115/1.4023650

Li, Z., Qin, L., Li, G., Sun, M., Du, P., Hu, H., Huang, X., & Chen, X. (2023) Numerical simulation on underwater vertical launching process under effect of initial gas. *Journal of Northwestern Polytechnical University, 41*(6), 1080-1088. https://doi.org/10.1051/jnwpu/20234161080

Liu, L., Zhang, Y., & Yuan, X. (2005). Numerical study of the flow field in underwater large-depth vertical launches. *Hydrodynamics Research and Progress: Series A,20*, (1), 90-94. https://doi.org/10.3969/j.issn.1000-4874.2005.01.015

Liu, Y., Lu, C., Li, J., & Cao, J. (2007). Study of ventilated air bubble flow during vertical launching of missile out of tube. *Hydrodynamics Research and Progress: Series A, 22*(5), 549-554. https://doi.org/10.3969/j.issn.1000-

4874.2007.05.004

Lv, Q. (2004). Application of nonlinear multi-objective optimal design in main engine selection. *Journal of Wuhan Shipbuilding Vocational and Technical College,* (03),22-25. https://doi.org/10.3969/j.issn.1671-8100.2004.03.007

Quan, X., Yan, G., Li, Y., Kong, D., & Li, M. (2014). Three-dimensional numerical study on the evolution process of tail bubble of underwater vehicle vertical launching. *Journal of Ship Mechanics*, *18*(7), 739–745. https://doi.org/10.3969/j.issn.1007-7294.2014.07

Shi, Y., Hua, Y., & Pan, G. (2020). Experimental study on the trajectory of projectile water entry with asymmetric nose shape. *Physics of Fluids, 32*(12), 122119. https://doi.org/10.1063/5.0033906

Shi, Y., Lu, J., Gao, S., & Yu, Y. (2023). Experimental study on motion interference characteristics of salvo water under influence of tube outlet. *Journal of Huazhong University of Science and Technology (Natural Science Edition), 51*(4), 18-23+54. https://doi.org/10.13245/j.hust.230403

Song, X., Wu, Q. G., Ni, B. Y., & Chen, H. L. (2019). Deformation and bubble entrapment of free surface before axisymmetric bodies detaching from water fully. *Journal of Mechanics, 35*(6), 863–874. https://doi.org/10.1017/jmech.2018.62

Wang, G., & Ostoja-Starzewski, M. (2007). Large eddy simulation of a sheet/cloud cavitation on a NACA0015 hydrofoil. *Applied Mathematical Modelling, 31*(3), 417–447. https://doi.org/10.1016/j.apm.2005.11.019

Wang, H., Li, Z., & Yan, X. (2019). Research on the effect of boat speed on the attitude of underwater vehicle launched underwater. *Ship Electronic Engineering, 39*(01), 135-138. https://doi.org/10.3969/j.issn.1672-9730.2019.01.033

Wang, H., Wu, Y., Cheng, D., & Yu, W. (2010). Analysis of ejection after-effects of submarine-launched simulated projectiles. *Ship Mechanics, 14*(10), 1122-1128. https://doi.org/10.3969/j.issn.1007-7294.2010.10.007

Yang, M., Wang, H., Zou, Z., Shen, L., Li, Y., Wu, B., Jiang, Y., & Liu, S. (2022). Experimental study of ventilation-assisted vehicle launched underwater flow. *Journal of Weapons and Equipment Engineering, 43*(12), 29-33+144. https://doi.org/10.11809/bqzbgcxb2022.12.005

You, T., Zhang, J., Wang, C., & Cao, W. (2011). Characteristic analysis of head flow field loading during the emergence process of a navigational body. *Journal of Beijing University of Aeronautics and Astronautics,* (05), 610-614. https://doi.org/10.13700/j.bh.1001-5965.2011.05.024.

Zhao, C. G., Wang, C., Wei, Y. J., & Zhang, X. S. (2015). An experimental study on characteristics of cavitation and ballistic of axisymmetric slender body underwater movement. *Journal of Physics: Conference Series, 656*(1). https://doi.org/10.1088/1742-6596/656/1/012175

Zhong, W., & Zhang, J. (2005). Underwater ballistic simulation of submarine-launched vehicles. *Journal of Ballistics*, (01), 8-12. https://doi.org/10.3969/j.issn.1004-499X.2005.01.002